Predicting the frequency of storm surges and extreme sea levels in the northwest Atlantic

N. B. Bernier[1] and K. R. Thompson[1]

Received 13 July 2005; revised 14 March 2006; accepted 30 May 2006; published 20 October 2006.

[1] A 40 year hindcast of storm surges in the northwest Atlantic and adjacent shelf seas is performed using a 2-D nonlinear barotropic ocean model forced by realistic 6 hourly winds and air pressures. This hindcast is used to generate spatial maps of the return level of storm surges and also to estimate the return period of extreme total sea levels. The accuracy of the hindcast is assessed in two ways. First, the standard deviation of the difference between the observed residuals (total sea level minus tide) and the hindcast is calculated at 24 tide gauge locations. A typical error standard deviation is 8 cm. Second, the 40 year return level of observed residuals is compared to that of the hindcast surges. The predicted 40 year return levels are typically within 10 cm of observed return levels at the 24 observation locations. A spatial map of the 40 year return level of surges is presented for the northwest Atlantic. It identifies the regions exposed to the largest surges. Total sea levels are reconstructed using (1) the hindcast surges and (2) tides and higher-frequency variability predicted from short, observed sea level records. An extremal analysis of the reconstructed total sea levels shows that their 40 year return levels are in good agreement (within about 10 cm) with the levels calculated from multidecadal observed sea level records. This means that given a short record anywhere within the model domain, or results from a good tidal model, 40 year return levels can be estimated.

Citation: Bernier, N. B., and K. R. Thompson (2006), Predicting the frequency of storm surges and extreme sea levels in the northwest Atlantic, *J. Geophys. Res.*, *111*, C10009, doi:10.1029/2005JC003168.

1. Introduction

[2] Global sea level is presently increasing at a rate of about 1 to 2 mm per year [*Houghton et al.*, 2001]. Over the next century, thermal expansion of the ocean is expected to increase global sea level by 0.11 m to 0.43 m [*Houghton et al.*, 2001]. The effects of glacier and ice sheet retreat, and permafrost thawing, are expected to increase the range of global sea level rise to 0.09 to 0.88 m with a central value of 0.48 m over the next century [*Houghton et al.*, 2001]. When considering the local increase of sea level with respect to the land (i.e., relative sea level rise), it is necessary to take into account the vertical motion of the Earth's crust due to processes such as glacio-isostatic rebound [e.g., *Peltier*, 2004] and tectonic movements [e.g., *Stollhofen et al.*, 2000]. The effect of vertical crustal motion can far exceed global sea level rise in some regions. In Fennoscandia, for example, the Earth's crust is rising so rapidly because of glacio-isostatic rebound that sea level is falling relative to the land at rates of up to 11 mm yr^{-1} [e.g., *Milne et al.*, 2001]. In the northwest Atlantic, glacio-isostatic movement is an important contributor to the change in relative sea level (Figure 1). Along the northeastern shores of Quebec isostatic rebound is causing relative sea level to fall at a rate of about 3 mm yr^{-1} while in the southern Gulf of St. Lawrence, it is causing an increase of about 3 mm yr^{-1} [*Peltier*, 2004]. Thus in the southern Gulf of St. Lawrence the combined effect of relative sea level rise and global sea level rise may lead to a relative sea level increase of order 1 m over the next century. This change is comparable to that of a large storm surge and so one can anticipate that the frequency and severity of flooding will increase significantly over the next century in this region.

[3] In addition to sea level rise, there are indications that storm severity may increase over the next century although the overall number of events may decrease [e.g., *Knippertz et al.*, 2000; *Lambert*, 2004]. Such an increase in severity has the potential to further exacerbate the problem of coastal flooding.

[4] The most widely used method for estimating the frequency of coastal flooding is based on the analysis of the observed annual maxima of long hourly sea level records using the classical theory of extremes [e.g., *Gumbel*, 1958; *Leadbetter et al.*, 1983; *Coles*, 2001]. Let M_n denote the maximum of a sequence of n independent, identically distributed (iid) random variables. (If the hourly sea level observations were independent, then in the present context n would be the number of hours in a year.) The Extremal Types Theorem [*Leadbetter et al.*, 1983] states that if location and scale parameters, a_n and $b_n > 0$ respectively, exist such that the probability $Pr[(M_n - a_n)/b_n < x]$ tends to a nondegenerate function, $G(x)$, then G is one of three extreme value types.

[1]Department of Oceanography, Dalhousie University, Halifax, Nova Scotia, Canada.

0148-0227/06/2005JC003168

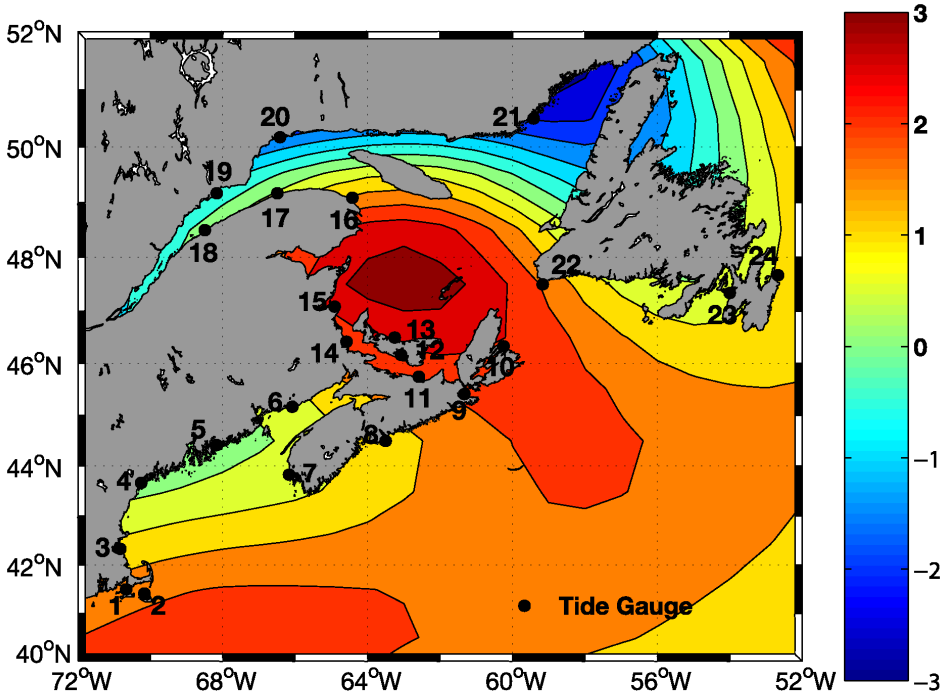

Figure 1. Rates of relative sea level rise (in mm yr^{-1}) according to the Ice-5G (VM2) model of Richard Peltier. Contours are shown every 0.5 mm yr^{-1}. Note the strong spatial variability with rates exceeding 3 mm yr^{-1} along the coast of New Brunswick and rates below −3 mm yr^{-1} along the northeastern shore of Quebec. Dots mark the locations of tide gauges that provided hourly sea level data for validation of the storm surge model. Numbers are station codes. Gauge names are listed in Table 1.

The Type I extremal distribution has the following form (see *Coles* [2001] for a review):

$$G(x) = \exp[-\exp(-x)] \tag{1}$$

On a return period plot, the critical level ($\eta_c = a_n + b_n x$) is plotted against a function of the return period Tr which is the reciprocal of the probability of an exceedance of η_c. The function is chosen such that if the maxima have a Type I extremal distribution, the relationship between η_c and Tr will fall on a straight line. The location parameter a_n shifts the return level line up or down; the scale parameter b_n controls the slope of the return level line. The limiting distribution of the maximum of a dependent sequence is the same as that of the corresponding iid sequence if stationarity is assumed and conditions are imposed to limit long-range dependence at high levels and the clustering of exceedances [e.g., *Leadbetter et al.*, 1983].

[5] The Type I distribution has proved very useful in the analysis of annual maxima of long hourly sea level records [e.g., *Dixon et al.*, 1998; *Lowe et al.*, 2001; *Woodworth and Blackman*, 2002; *Unnikrishnan et al.*, 2004; *Bernier et al.*, 2006]. In practice a_n and b_n are estimated from the ordered sequence of observed annual maxima for a given location using the method of maximum likelihood [e.g., *Coles*, 2001]. This allows probabilities of exceedance to be estimated for η_c that exceed the largest observed annual maximum. It is often easier to interpret this probability in terms of its reciprocal which is simply the return period or equivalently the average time between exceedances of η_c in years. The method can be adapted to allow for nonstationarity in the annual maxima by allowing the location and scale parameters to change with time: e.g., $a_n = a_{n0} + a_{n1}t$ where t denotes time and a_{n0}, a_{n1} are parameters estimated from the observed annual maxima. This approach has been used to describe time variation in extremes [e.g., *Dixon and Tawn*, 1999; *Coles*, 2001] and allows the concept of return periods to become time dependent.

[6] A major problem with the application of the classical method of extremes is that typically 30 or more annual maxima are required to reliably estimate a_n and b_n. For many locations such data are not available. This has stimulated the development of methods for estimating return periods from short records. In a pioneering study, *Pugh and Vassie* [1980] (and later *Tawn and Vassie* [1989]) tackled the problem by writing the instantaneous sea level (η) as the sum of a tidal component (η_T) and a residual (η_R):

$$\eta = \eta_T + \eta_R \tag{2}$$

[7] The residual includes the effect of observation and tidal prediction errors and also physical processes such as river input to continental shelf seas, storms, and harbor seiches. The basic idea of the [*Pugh and Vassie*, 1980] approach is to convolve the histograms of the tide and

Table 1. Tide Gauge Locations and Statistics of Sea Level Variability[a]

Station Name	Code	Trend	a_{n1}	$\sigma_{\mathcal{L}\eta_R}$	σ_{η_S}	γ^2	$\sigma_{(\mathcal{L}\eta_R-\eta_S)}$
Woods Hole	1	**2.5**	−4.2	0.12	0.12	0.33	0.06
Nantucket Island	2	**2.6**	0.8	0.11	0.11	0.39	0.06
Boston	3	**2.5**	−2.8	0.13	0.12	0.32	0.06
Portland	4	**1.8**	−1.5	0.12	0.13	0.34	0.06
Bar Harbor	5	**2.1**	−1.5	0.11	0.12	0.35	0.06
Saint John	6	**2.2**	1.3	0.11	0.11	0.52	0.07
Yarmouth	7	**2.8**	−3.2	0.11	0.12	0.37	0.06
Halifax	8	**3.2**	−1.6	0.11	0.12	0.37	0.06
Point Tupper	9	**1.9**	−3.5	0.11	0.12	0.51	0.07
North Sydney	10	**2.8**	−2.6	0.11	0.12	0.51	0.07
Pictou	11	**2.6**	3.2	0.17	0.16	0.42	0.09
Charlottetown	12	**3.1**	−2.0	0.16	0.15	0.51	0.10
Rustico	13	**2.4**	2.1	0.15	0.16	0.49	0.10
Shediac Bay	14	**1.7**	12.2	0.20	0.16	0.43	0.11
Lower Escuminac	15	**2.0**	−4.8	0.16	0.13	0.41	0.09
Rivière−au−Renard	16	−0.3	−2.9	0.14	0.13	0.45	0.08
Sainte−Anne−des−Monts	17	**−0.7**	**−8.8**	0.16	0.14	0.42	0.09
Pointe−au−Père	18	**−1.2**	−0.3	0.17	0.14	0.35	0.09
Sept−Iles	19	**1.8**	−4.7	0.16	0.14	0.38	0.09
Baie−Comeau	20	**−6.0**	−8.4	0.18	0.14	0.35	0.09
Harrington Harbor	21	**−0.9**	−0.7	0.12	0.12	0.55	0.08
Port−aux−Basques	22	**2.2**	−1.2	0.12	0.12	0.45	0.07
Argentia	23	**1.8**	−4.0	0.12	0.13	0.63	0.08
St John's	24	**1.9**	1.5	0.13	0.15	0.55	0.09

[a]Observed and modeled sea level variability at the tide gauge locations. The columns are defined as follows: (1) station name, (2) station code, (3) linear trend in the annual means, in mm yr^{-1}, calculated using all available years (i.e., includes data outside of the hindcast period when available); bold if significantly different from 0 at the 5% significance level, (4) trend in location parameter a_{n1} (in mm yr^{-1}, see text) on the basis of 1960–1999 adjusted annual maxima, (5) standard deviation (in meters) of the filtered residuals for the stormy season (September to April), (6) standard deviation (in meters) of the surge hindcast for the stormy season, (7) γ^2, the ratio of the variance of the error ($\mathcal{L}\eta_R - \eta_S$) upon the variance of the filtered residuals $\mathcal{L}\eta_R$ for the stormy season, and (8) standard deviation (in meters) of the hindcast error $\sigma_{(\mathcal{L}\eta_R-\eta_S)}$ for all seasons combined.

residual to obtain an estimate of the histogram of the total level η. The advantage of the convolution is that it gives a histogram for η that has a wider range than the original sea level observations. The reason is that the largest residual may not have occurred at the highest tide in the record but the convolution approach allows for this possibility. *Pugh and Vassie* [1980] show that the convolution approach can give useful 50 year return levels from just a few years of hourly sea level data if tide-surge interaction is negligible.

[8] In the present study we examine the return period of extreme sea levels focusing on the continental shelf seas bordering the northwest Atlantic. In contrast to classical extremal analysis theory, we use a dynamically based model to predict the effect of storms on coastal sea level. Our approach is similar to that used by *Flather et al.* [1998] and *Kaas et al.* [2001] and proposed by *Soares et al.* [2002] for the European shelf seas. The dynamically based approach has several advantages. First it allows predictions of return periods to be made at locations for which no sea level observations are available and for which the classical methods are therefore inapplicable. Second, projections of return periods can be made under assumed climate change scenarios that involve changes in the frequency and severity of storms.

[9] The outline of the paper is as follows. Sea level observations from 24 coastal tide gauges from the northwest Atlantic are described in section 2 including their annual means, annual maxima and seasonality. The storm surge model and its forcing fields are described in section 3 along with a hindcast of sea level variability for the period 1960–1999. The hindcast is validated using the hourly sea level observations. The return periods of extreme sea levels are discussed in Section 4. The results of the study are summarized and discussed in section 5.

2. Description of Sea Level Observations

[10] The initial set of sea level observations analyzed in this study was recorded by 36 tide gauges located along the east coast of Canada and the northeastern United States. The Canadian data were provided by the Marine Environmental Data Service (http://www.meds-sdmm.dfo-mpo.gc.ca) and the U.S. data by the Center for Operational Oceanographic Products and Services (http://www.co-ops.nos.noaa.gov/). All sea level records, before and after removal of the tidal signals, were carefully scrutinized for errors prior to analysis. In particular, the data were plotted and visually checked for anomalous spikes, timing errors (evident as significant bursts of tidal energy in the residuals), and datum shifts. Suspect observations were removed from the records. A few stations were rejected from this study on the basis of long sequences of large tidal signals in the residuals (e.g., Eastport, Maine) or multiple datum shifts (e.g., West Ste-Modeste, Newfoundland). Stations with less than 10 years of corrected data within the 40 year hindcast period were also removed from the analysis. Following the quality control, 24 tide gauge records remained for analysis (Figure 1 and Table 1). The data availability for each gauge record is shown in Figure 2. Note that there are numerous short interruptions that are not visible in this figure because of the limited resolution along the time axis.

2.1. Annual Means and Maxima

[11] Time series of the annual means for two representative stations, Boston and Harrington Harbor, are shown in Figure 3 (left). (Note that this is the only time we will discuss

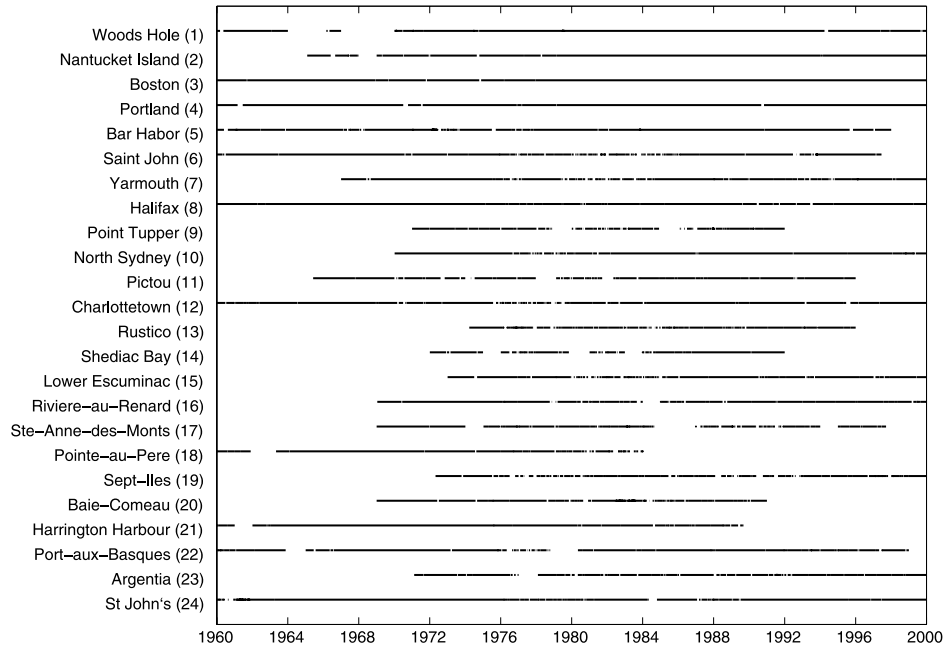

Figure 2. Availability of tide gauge data for the 1960–1999 hindcast period. Stations are marked along the y-axis (locations are shown in Figure 1). Time is indicated along the x-axis. The lines indicate periods for which there were observations. Note that numerous small gaps in some records are not visible.

data outside of the hindcast period.) Well defined linear trends are clearly evident at both stations. Sea level is slowly rising at about 2.5 mm per year at Boston while at Harrington Harbor it is falling at about 0.9 mm per year. The rates of rise of annual mean sea level are given in Table 1 for all 24 gauges. They vary considerably from station to station, with relative sea level generally falling in the St. Lawrence River and increasing along the Atlantic Coast. Although the

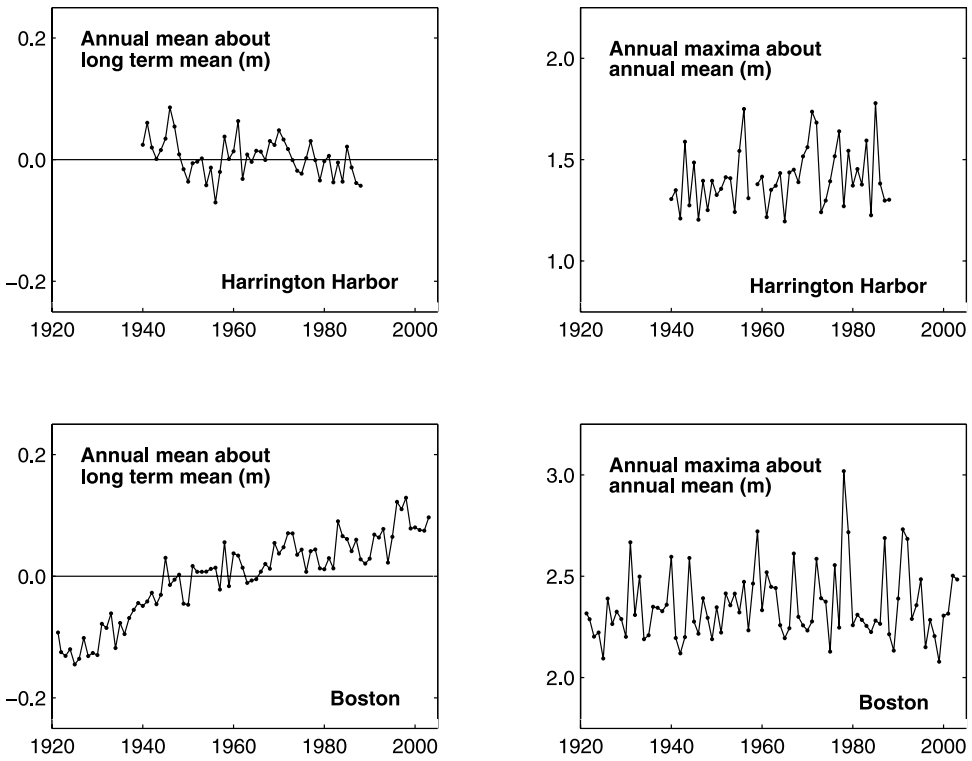

Figure 3. Observed annual mean sea levels and annual maxima for two representative locations. Long-term mean sea level has been removed from the annual means (left column). Right column shows the annual maxima about the corresponding annual means. Average difference between the means and maxima is due in large part to the tides.

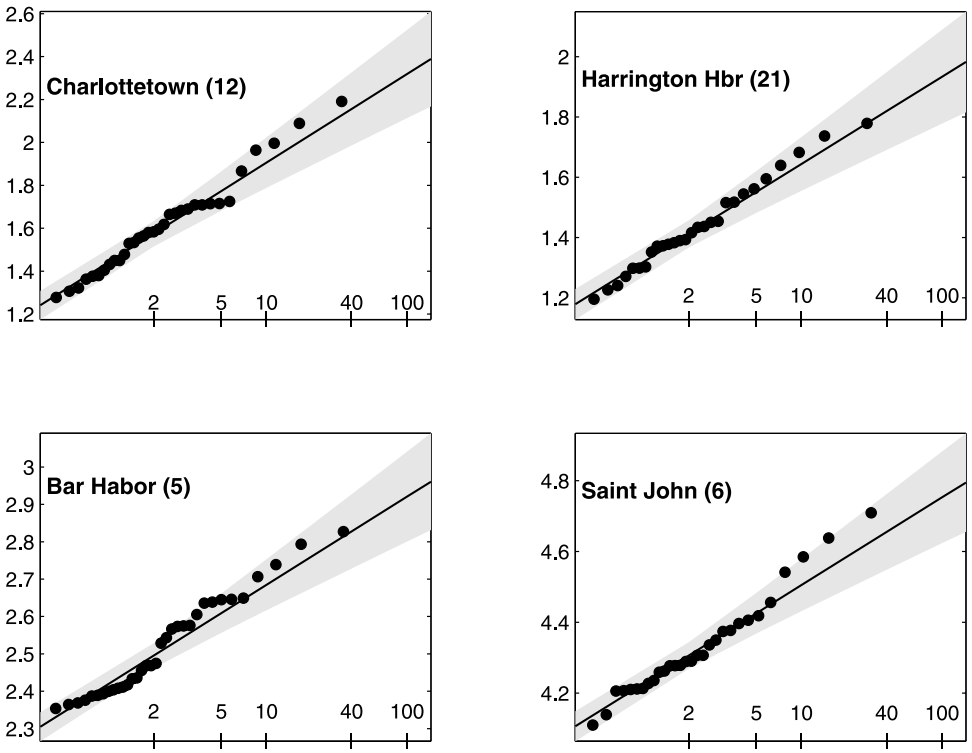

Figure 4. Return period of extreme sea levels for four representative stations. Return period in years is marked along the x-axis. Y-axis is the return level in meters. Dots are the ordered, observed annual maxima (about the annual mean) available between 1960–1999. Return level lines were fitted using maximum likelihood. Shaded areas mark the 95% confidence intervals for the return level. Note changes in the scale of the y-axis.

rates are based on short records and are subject to significant interdecadal variations, the overall spatial pattern generally agrees with the rates predicted by *Peltier* [2004] as shown in Figure 1.

[12] The annual maxima about the corresponding annual mean (henceforth the adjusted annual maxima) for the two representative stations are also plotted in Figure 3. Using the method discussed in section 1, the linear trends in the location parameter of the Type I extremal distribution for Boston and Harrington Harbor are estimated to be -2.8 mm yr^{-1} and 0.7 mm yr^{-1} respectively. Neither trend is significantly different from 0 at the 5% significance level. A similar analysis for the remaining stations reveals that only 1 station has a trend that is significantly different from 0 (Table 1). However, it is noticeable that 18 out of 24 stations have negative trends with a median rate of -1.8 mm yr^{-1}. This suggests that for this region, there has been a slight but large spatial-scale decrease in the extremes over the period 1960–1999. We will return to the interpretation of these results in section 3.3 after we have discussed the surge hindcast.

[13] The adjusted annual maxima for 4 representative stations are plotted on Type I probability paper in Figure 4. The y-axis shows the critical level and the x-axis shows the corresponding return period (see section 1). The dots are the ordered annual maxima and the shaded area mark the 95% confidence intervals obtained using the delta method [e.g., *Coles*, 2001]. The closer the points to a straight line, the stronger the evidence that the underlying probability distribution is a Type I distribution. Overall, the results suggest that the assumption of a Type I distribution is reasonable.

[14] The return levels at the shortest return periods are determined primarily by the tides. At Saint John where the tidal amplitude regularly exceeds 4 m, the 2 year return level is 4.26 m; at Harrington Harbor where the tides rarely exceed 1.15 m, the 2 year return level is only 1.36 m. For long return periods, the return levels are due to the combined effect of large tides and large surges. This implies that the slope of the lines running through the annual maxima (Figure 4), or equivalently the difference between the 40 year and the 2 year return levels, is controlled by the probability distribution of the large surges. As will be shown later, the slopes are largest in the southern Gulf of St. Lawrence where surges are typically largest (e.g., Charlottetown).

[15] The 40 year return level of total sea level for each station is plotted in Figure 5a. The shaded area marks the 95% confidence interval based on fitting the Type I distribution. The widest confidence intervals are associated to stations with short records (e.g., Shediac with only 12 observed annual maxima). As expected, the largest 40 year return levels are observed at stations with large tidal amplitudes (e.g., Saint John in the Bay of Fundy).

2.2. Residuals

[16] The residual is simply the difference between the observed sea level and the predicted tide, $\eta_R = \eta - \eta_T$. To calculate η_T for each station, a tidal analysis was first performed on a year by year basis to give the yearly tide, η_{Ta}. The analysis was based on the standard set of 68 tidal constituents fit to the observations using the tidal analysis

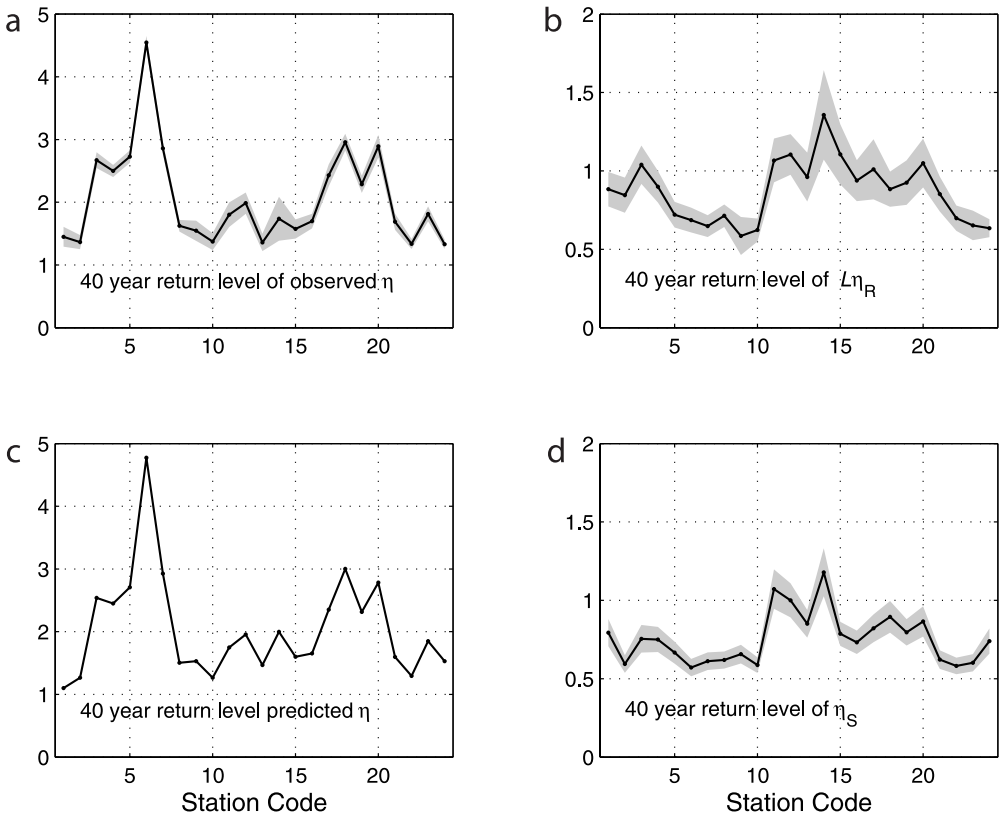

Figure 5. 40 year return level of total sea levels and residuals. X-axis shows the station code. Y-axis is the 40 year return level in meters calculated from the Type I distribution fitted to the adjusted annual maxima (Figure 4). Shaded areas mark the 95% confidence intervals. (a) The observed 40 year return levels. (c) The 40 year return level obtained using 5 years of hourly sea level observations and the 40 surge hindcast (section 4). (b) The 40 year return level of the filtered residuals ($\mathcal{L}\eta_{\mathcal{R}}$). (d) The 40 year return level of the hindcast surges (η_S).

package of *Pawlowicz et al.* [2002]. It soon became clear that this approach failed to remove all of the tidal energy from the sea level records. We therefore performed an additional tidal analysis on the residuals on a month by month basis (η_{Tm}), using only constituents with a signal-to-noise ratio greater than unity. This is a way of band-pass filtering the residuals in the vicinity of the tidal frequencies. (The monthly means were therefore removed separately.) To check that we were not overfitting the tides, we performed the same monthly tidal analysis on some of the hindcast surges (section 3). As expected, the monthly analyses failed to remove significant energy confirming that the energy removed from the sea level residuals was primarily tidal in origin.

[17] The surge model (section 3) is driven by winds and pressures provided every 6 hours. This corresponds to a Nyquist frequency of one cycle every 12 hours. Thus apart from the contribution from nonlinear effects, the surge model will not generate significant variability at periods shorter than 12 hours. To compare the surge model output and the observed residuals we therefore removed variability in the residuals at periods shorter than 12 hours using a low-pass filter. This filter removed for example the effect of high-frequency winds and seiches, both of which can be important [*Pugh*, 1987] but are not represented by the surge model. We denote the low-pass-filtered residual by

$$\mathcal{L}\eta_{\mathcal{R}} = \mathcal{L}(\eta - \eta_{\mathrm{Ta}} - \eta_{\mathrm{Tm}}) \tag{3}$$

[18] The calculation of $\mathcal{L}\eta_{\mathcal{R}}$ is illustrated in Figure 6 for Boston. Figure 6 (top) shows the observed sea level about the annual mean. Figure 6 (middle) shows η_{Ta}, and the difference between η and η_{Ta}. The difference clearly shows energy at both tidal and high frequencies. Figure 6 (bottom) shows $\eta_{Ta} + \eta_{Tm}$, the predicted tide, and the low-pass-filtered residuals, $\mathcal{L}\eta_{\mathcal{R}}$. Note that the processing of the residuals, as shown in this example, has not led to unrealistic damping of large surges.

[19] To examine the distribution of large surges in the study area we performed an extremal analysis on $\mathcal{L}\eta_{\mathcal{R}}$, following exactly the same steps taken in the extremal analysis of the total water levels described in the previous subsection. (Results will be compared to an extremal analysis of the modeled surges later.) The annual maxima of the residuals were found to lie close to a straight line, indicating that the Type I distribution is also a reasonable model for the distribution of the large residuals (not shown). The slope of the return level lines also increases with the variability of the surges. Note however, that scaling the

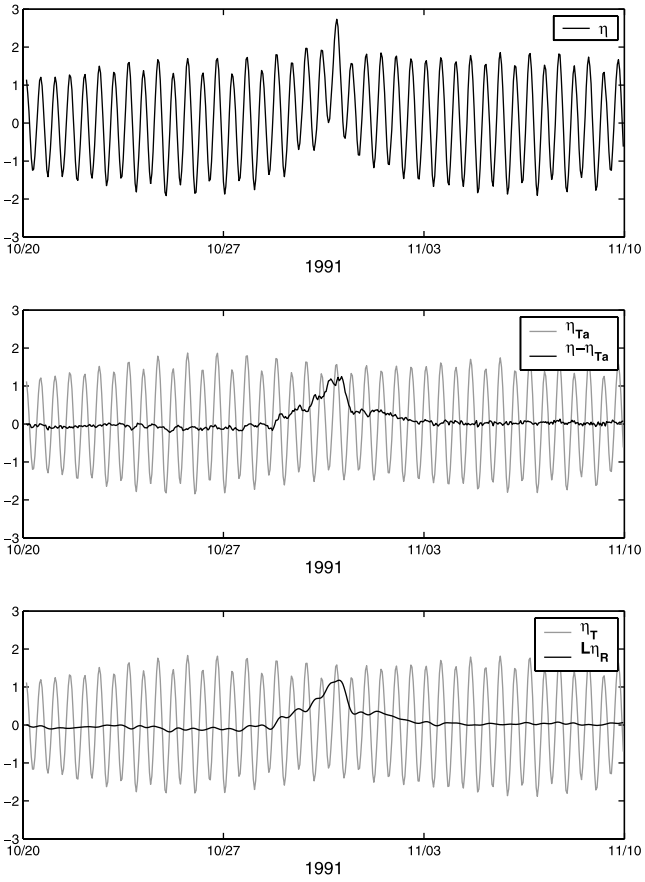

Figure 6. Decomposition of the observed sea level at Boston. (top) Observed sea level in meters relative to the annual mean. (middle) Annual tide η_{Ta} (light line) and $\eta - \eta_{Ta}$. (bottom) Total tide $\eta_T = \eta_{Ta} + \eta_{Tm}$ (light line), where η_{Tm} is the monthly tide and $\mathcal{L}\eta_{\mathcal{R}}$ is the filtered residual. This figure also highlights how large surges at or near high tide typically lead to extreme events. If this large surge had occurred 6 hours earlier or later (i.e., at low tide), then the total sea level would not have corresponded to an annual maximum. Thus the largest residuals in a year do not always lead to an annual maximum because they may fail to coincide with high tide.

slope of the lines by the standard deviation of the filtered residuals does not explain the difference in slopes between stations. The standard deviation alone is therefore not the key to the differences in slope; the differences also depend on additional features of the residual probability distribution.

[20] The 40 year return levels of $\mathcal{L}\eta_{\mathcal{R}}$ and their 95% confidence intervals are plotted in Figure 5b for each station. As before, stations with wide confidence intervals are those with the shorter records. The largest residuals generally occur in the Gulf of St. Lawrence and the smallest residuals occur around southwest Newfoundland. Note also the difference in the spatial structure of the extreme total sea levels and residuals (compare Figures 5a and 5b). This difference is not only due to differences in surge amplitude; it is also due to large spatial differences in tidal amplitudes.

[21] In general, the largest residuals occurred between September and April inclusive (hereafter the stormy season). To quantify the seasonal variability, the standard deviation of the residuals ($\sigma_{\mathcal{L}\eta_{\mathcal{R}}}$) for each station and for each month was calculated. Thus for a complete 40 year record, we have 40 $\sigma_{\mathcal{L}\eta_{\mathcal{R}}}$ for each month of each year for a total of 480 values. Box plots of $\sigma_{\mathcal{L}\eta_{\mathcal{R}}}$ for January through December, for Boston are shown in Figure 7. Typical $\sigma_{\mathcal{L}\eta_{\mathcal{R}}}$ for each month are represented by the line cutting approximately through the center of the box (marking the median). Following these lines from month to month reveals a seasonal cycle in surge variability with the larger surges occurring during the stormy season. Taken individually, the height of each box (a measure of the spread in $\sigma_{\mathcal{L}\eta_{\mathcal{R}}}$) is an indicator of interannual variability. In January the height of the box is more than twice that of July indicating that year to year variability in the residuals is much stronger in winter than in summer. Similar results were found for the remaining stations demonstrating that the residual variability in this region varies significantly both seasonally and interannually.

3. Hindcast of Northwest Atlantic Storm Surges

[22] In the next section the surge hindcasts are combined with tidal predictions to test our ability to hindcast extremes in total sea level. We now describe the storm surge model, the wind and air pressure fields used to force it, and the accuracy of the surge hindcasts. The quality of the hindcast is assessed by comparison with the statistics presented in the previous section.

3.1. Storm Surge Model

[23] The storm surge model is a modified version of the Princeton Ocean Model [*Mellor*, 1998] and is based on the following depth averaged, barotropic momentum and continuity equations:

$$\frac{\partial \mathbf{u}}{\partial t} + \mathbf{u}\cdot\nabla\mathbf{u} + \mathbf{f}\times\mathbf{u} = -\mathrm{g}\nabla\eta_{\mathrm{W}} + \frac{\boldsymbol{\tau}_{\mathrm{s}} - \boldsymbol{\tau}_{\mathrm{b}}}{\rho \mathrm{h}} + \mathrm{A}\nabla^2\mathbf{u} \quad (4)$$

$$\frac{\partial \eta_W}{\partial t} + \frac{\partial (Hu)}{\partial x} + \frac{\partial (Hv)}{\partial y} = -\frac{\partial \eta_P}{\partial t} \quad (5)$$

where $\mathbf{u} = (u, v)$ denotes the depth-averaged horizontal velocity, $\mathbf{f}$ is the upward pointing unit vector scaled by the Coriolis parameter, $\boldsymbol{\tau}_s$ and $\boldsymbol{\tau}_b$ are the surface and bottom stress, h is the mean water depth, A is the horizontal viscosity, and H is the total water depth. The rest of the notation is standard. The slightly nonstandard feature of these equations is that the model's sea level (η_S, where the subscript s denotes surge) has been written in the form [e.g., *Gill*, 1982]

$$\eta_S = \eta_P + \eta_W \quad (6)$$

where η_P is the inverse barometer effect due to variations in air pressure and η_W is the isostatically adjusted sea level of the model. η_W is due to the effect of the wind and the dynamic response of sea level to air pressure forcing. The model is formulated such that η_W is the prognostic variable [*Bobanović*, 1997].

[24] The surface wind stress is computed from the wind at 10 m. The kinematic stress magnitude is given by $c_d(W)W^2$ where W is the wind speed and c_d is a drag coefficient that equals 1.2×10^{-3} for $W < 8$ m s^{-1} and thereafter increases

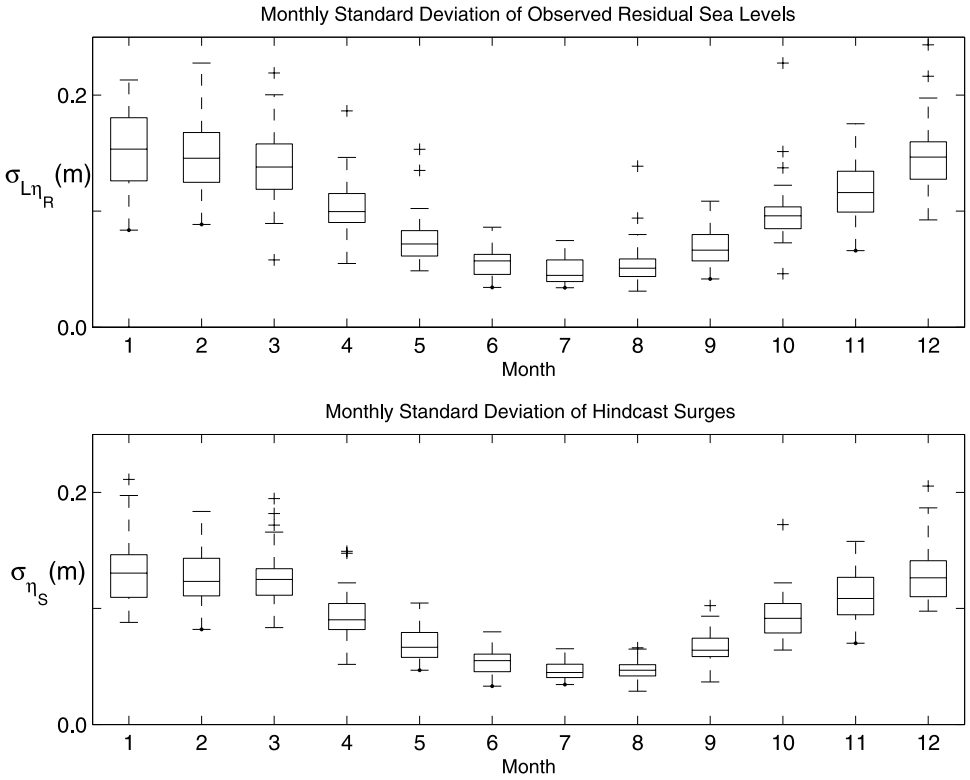

Figure 7. Monthly variation of observed residuals and hindcast surges at Boston. Standard deviations of the residuals ($\sigma_{\mathcal{L}\eta_{\mathcal{R}}}$) and surge hindcast ($\sigma_{\eta_S}$) were calculated for each month of each year of the 40 year hindcast period. There are therefore potentially 40 standard deviations for each of the 12 months of the year. The figure shows box plots of the standard deviations for each month. In each month, the box plots have lines at the lower quartile, median and upper quartile. Outliers, which extend beyond the whiskers are shown as crosses. (top) Standard deviation of $\mathcal{L}\eta_{\mathcal{R}}$. (bottom) Standard deviation of η_S.

linearly by 0.065×10^{-3} for every 1 m s^{-1} increase in W. The bottom stress formulation is of the form $c_{db}\mathbf{u}(u^2 + v^2)^{1/2}$ where c_{db}, the bottom drag coefficient, equals 2.5×10^{-3}.

[25] The model domain extends from 38°N to 60°N and 72°W to 42°W. It includes the Labrador and Newfoundland Shelves, Gulf of St. Lawrence, Scotian Shelf, Bay of Fundy and Gulf of Maine. The model resolution is 1/12° which corresponds to a latitudinal resolution of about 9 km. The bathymetry was derived from a combination of the ETOPO-5 database supplemented by soundings that were manually edited to better represent the coastline [*Bobanović*, 1997]. A standard radiation boundary condition is applied to the model's open boundaries according to which the depth-averaged velocity normal to the boundary is equated to $\sqrt{g/h}\,\eta_W$ [*Davies and Flather*, 1978]. This is equivalent to radiating about the isostatically adjusted sea level at the open boundary.

3.2. Forcing Fields

[26] The winds used to drive the model were obtained from the AES40 data set [*Swail and Cox*, 2000]. The fields cover the North Atlantic (0° to 75°N, 83°W to 20°E) and are available every 6 hours from 1958 to 2000 with a horizontal resolution of 0.625° in latitude and 0.833° in longitude. The generation of the AES40 winds by *Swail et al.* [2000] are a combination of first guess fields from the NCEP/NCAR reanalysis [*Kalnay et al.*, 1996] and the reassimilation of some 200,000 wind observations. These fields were first evaluated and adjusted by trained meteorologists on the basis of comparison with wind observations. The adjusted fields were then further modified after assessing the performance of a wave model driven by the adjusted winds. In total over 10,000 hours were spent by the meteorologists subjectively improving the NCEP reanalysis winds. Validation studies suggest that the AES40 winds have a bias of about 0.3 m s^{-1} and an RMS error of about 1.2 m s^{-1} [*Swail et al.*, 2000].

[27] Unfortunately surface air pressure fields were not included in the AES40 data set. For the present study it is important that the model be forced by air pressure fields with the same spatial and temporal resolution as the winds. We therefore used the wind fields to dynamically infer the surface pressure fields using the approach described in Appendix A. The RMS errors of the inferred air pressures, on the basis of comparison with independent observations from land and ocean stations, is less than 3 mb [*Bernier*, 2005]. This corresponds to an isostatically adjusted sea level error of 3 cm which is considered acceptable for the purposes of the present study.

3.3. Validation of the Storm Surge Hindcast

[28] The storm surge model was run for the period 1960 to 1999, driven by the AES40 winds and inferred air pressures. The monthly means were then removed to allow direct comparison with $\mathcal{L}\eta_{\mathcal{R}}$. Overall there was generally

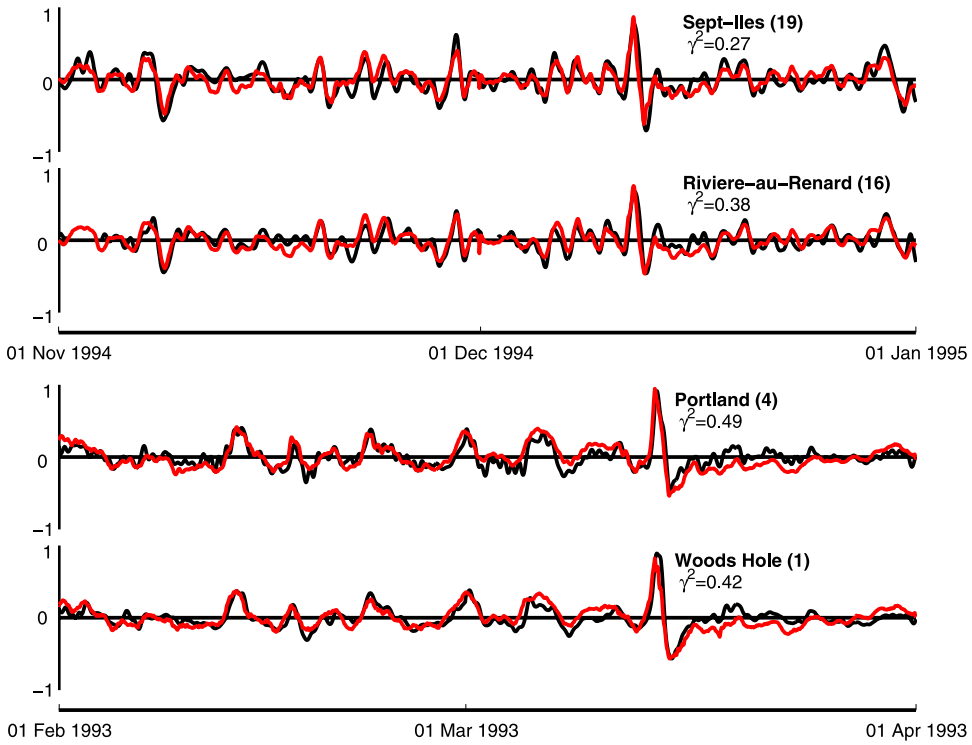

Figure 8. Illustration of the predictive skill of the model for two storms. Filtered residuals, $\mathcal{L}\eta_{\mathcal{R}}$, are plotted in black and the surge hindcasts, η_S, are plotted in red for four representative stations. The γ^2 values are a measure of the forecast skill. The series shown here illustrate an average fit (see Table 1).

good agreement between the surge hindcasts (η_S) and the observed sea level residuals ($\mathcal{L}\eta_{\mathcal{R}}$) as illustrated in Figure 8. Clearly, the model reproduces well the amplitude of these two large storm events. The frequency-dependent structure of η_S also generally compares well with that of $\mathcal{L}\eta_{\mathcal{R}}$ (the power spectral comparison is not shown). Figure 8 also shows the γ^2 statistics for the four stations. It is the ratio of the variance of the hindcast errors to the variance of the observations [e.g., *Thompson et al.*, 2003]

$$\gamma^2 = \frac{\mathrm{Var}(\mathcal{L}\eta_{\mathcal{R}} - \eta_S)}{\mathrm{Var}(\mathcal{L}\eta_{\mathcal{R}})} \tag{7}$$

[29] The γ^2 values of the series presented in Figure 8 are typical of the values found for other times and stations. The γ^2 of the stormy season for each of the 24 tide gauges are given in Table 1. On the basis of these γ^2, the model generally performs better at locations along the Scotian Shelf and along the northeastern U.S. coast. The higher γ^2 around the southern Gulf of St. Lawrence may be explained by the quality of the wind hindcasts in this region where strong orographic effects [e.g., *Bowyer and Gray*, 1995] may not be resolved by the AES40 winds.

[30] We were encouraged to find that γ^2 remained relatively constant when calculated separately for each year of the 40 year hindcast. The standard deviation of the forecast error is also generally constant (typically less than 10 cm, Table 1). This implies that the accuracy of AES40 winds and the inferred air pressures are fairly stable over the study period.

[31] The standard deviation of the model hindcasts agree well with the standard deviation of $\mathcal{L}\eta_{\mathcal{R}}$ at the 24 tide gauges (Table 1) for the stormy season. This is illustrated in Figure 7 where the observed seasonal variability (top) for Boston compares well with the modeled seasonal variability (bottom). This encouraged us to generate maps of the standard deviation of the surge hindcasts for each season (Figure 9). Spring (April, May, June) and Summer (July, August, September) are relatively quiet. Note also the large spatial differences within seasons. Overall, the Gulf of St. Lawrence and the Labrador Shelf have the largest surges.

[32] The focus of the present study is the distribution of extreme surges and sea levels. This means that although small errors in the timing of hindcast surges may lead to large hindcast errors, and thus a large value of γ^2, such timing errors will have little effect on the extreme surges. To validate the model with respect to extreme surges, we compared the 40 year return level of η_S, calculated from a Type I extremal analysis, with the 40 year return level of $\mathcal{L}\eta_{\mathcal{R}}$ (Figure 5d).

[33] The predicted return levels have a spatial pattern that is similar to the observed return levels. There is a slight tendency to underestimate the 40 year return level, but we were encouraged to find that our estimates are usually within the confidence interval of the observed return levels. The differences are most evident at Boston, St. John's, and Shediac Bay (compare Figures 5b and 5d). At Boston, two of the largest events are associated with hurricanes. In general, the resolution of our forcing fields is too coarse to resolve hurricanes. At Boston and St. John's, differences may also be due to horizontal model resolution and the difficulty

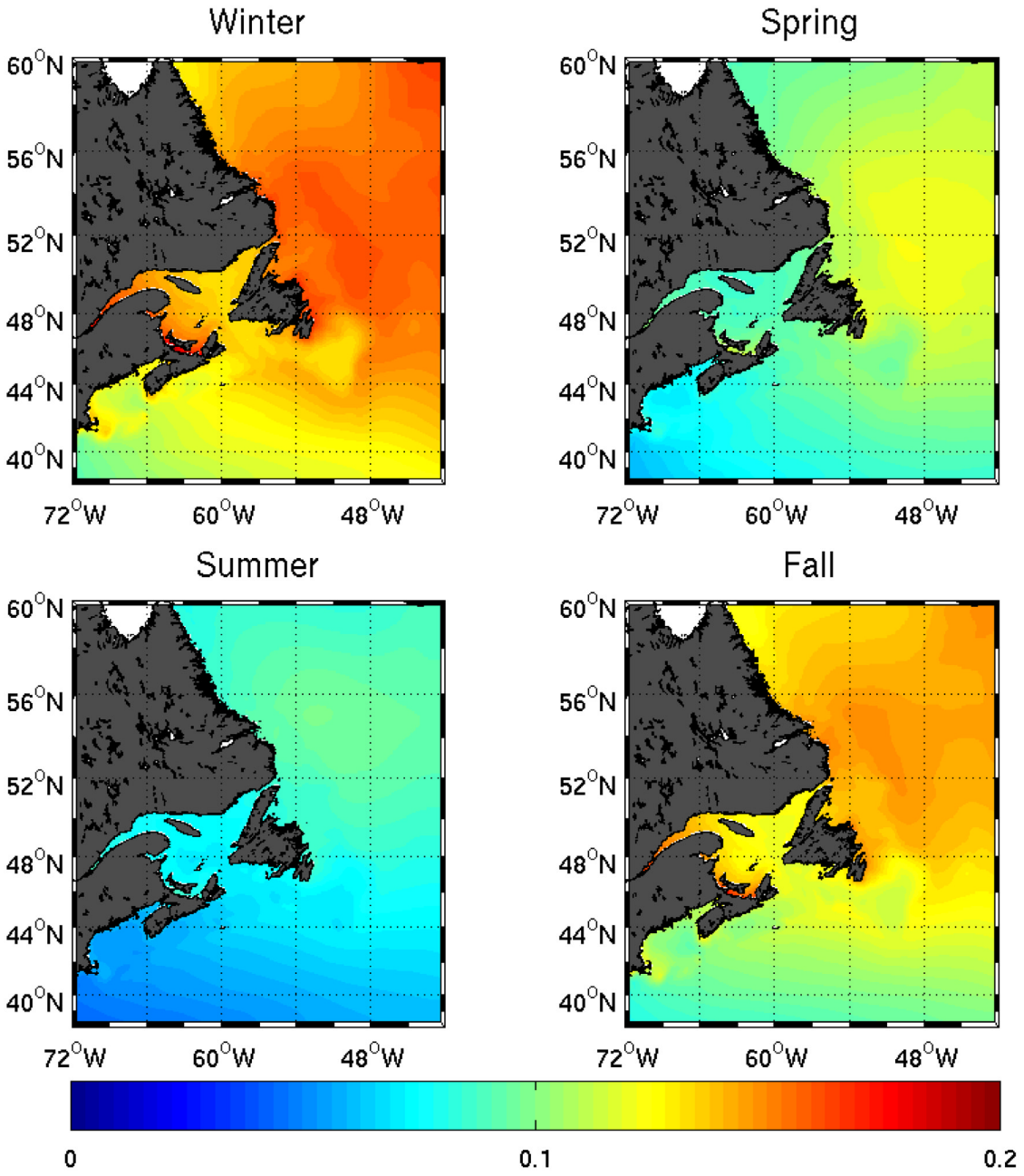

Figure 9. Seasonal variation of the standard deviation of the hindcast surges. Colorbar indicates the standard deviation in meters. Four seasons are: winter (January, February, March), spring (April, May, June), summer (July, August, September), and fall (October, November, December).

associated with modeling harbor effects. For example, the effect of wind setup at small scales, e.g., the scale of a harbor or coastal inlet, is not captured by the storm surge model. Such setup, on the basis of a scale analysis of the dynamical equations and the long coherence scales of the sea level residuals, is generally expected to be small on timescales of hours to days. However, it should be noted that during periods of extremely intense winds such set-up effects can be large. For example, the observed residual sea level in Bedford Basin (Halifax) was some 30 cm higher than the sea level observed at the Halifax tide gauge located in the harbor (the two gauges are roughly 1 km apart) during the passage of Hurricane Juan (D. Mercer, personal communication, 2006). In general, the largest surges rarely happen at high tide. It is therefore possible to reconstruct total sea levels well without including localized wind set-up effects. At Shediac Bay the difference in return levels could be the result of comparing an extremal analysis based on a 12 year record to an extremal analysis based on a 40 year record.

[34] Given the overall reasonable agreement between the return periods of the observed residuals and model hindcasts we made a map of the 40 year return level for the study area (Figure 10). It is the first time such a map has been generated. This map was obtained by fitting a Type I distribution to the 40 annual maxima at every grid point. Figure 10 highlights the spatial variability in the 40 year return levels.

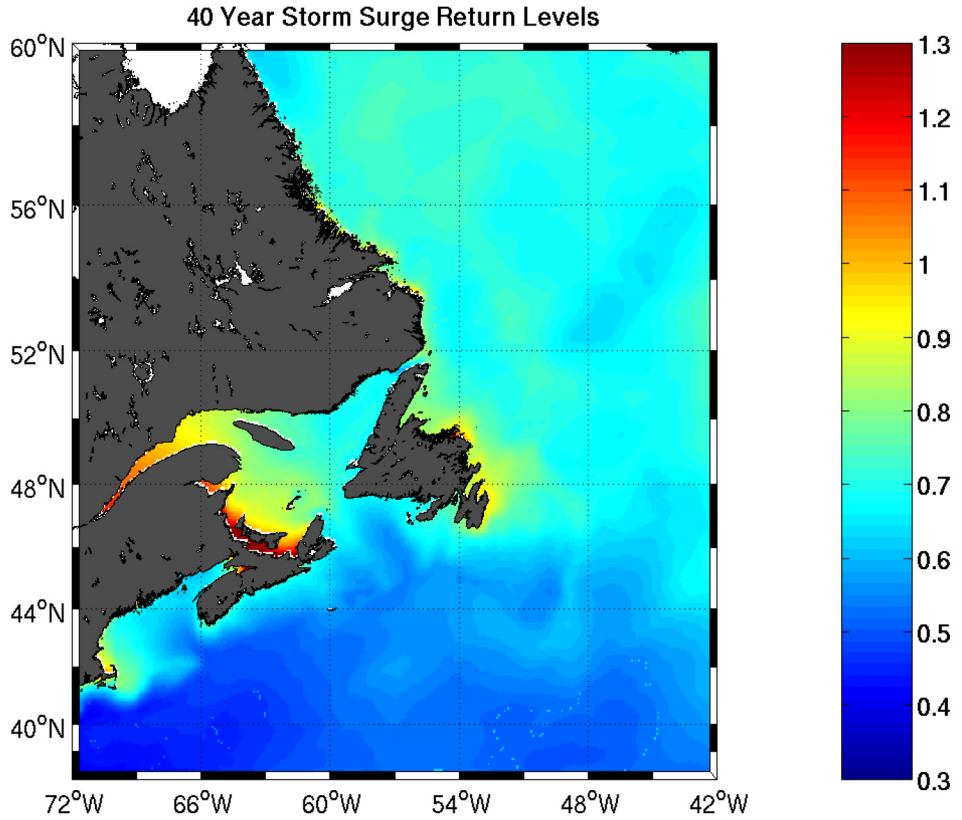

Figure 10. 40 year return level of extreme storm surges based on the surge hindcast. Colorbar indicates the 40 return levels in meters.

[35] Finally, trends in the location parameter ($a_n = a_{n0} + a_{n1}t$, see section 1) were calculated at every grid point of the hindcast. In general, the trend is negative over the entire region except over the Labrador Shelf and Sea and the northeastern Gulf of St. Lawrence. Although few grid points have trends significantly different from zero, they together suggest a decrease in the intensity of extreme events. Negative trends were also found at most tide gauge locations (Table 1). These findings lead us to conclude that the region has likely seen a small reduction in extreme events between 1960 and 1999, because of changes in atmospheric conditions. We return to this point in section 5.

4. Return Period of Total Sea Levels

[36] Given an observed hourly sea level record longer than about 30 years, it is straightforward to estimate the return period of extreme events using a standard Type I extremal analysis as described above. Difficulties arise when return periods are required for locations with short records (less than 5 years say) or, in the extreme, when no data are available. In this section we outline how such difficulties can be overcome by taking advantage of hindcasts from a storm surge model.

4.1. Return Periods From Short Records

[37] The basic idea behind our approach is simple: add the multidecadal storm surge hindcast to tidal predictions for the hindcast period (calculated using tidal constants from the short record) and subject the reconstructed total sea level record to a standard extremal analysis based on its annual maxima. We stress that modeling the exact occurrence of a given extreme is not the goal; we rather focus on our ability to reproduce the distribution of the annual maxima and thus the return period of extreme sea levels.

[38] We begin by assuming a 5 year sea level record is available. The first step is to predict the tide for the 5 year period based on tidal constants fit to just one of the 5 years. (We used the tidal analysis package of *Pawlowicz et al.* [2002] and selected 1990 as the default analysis year given its generally good data coverage. Note stations 17, 18, 19, and 21 had significant data gaps, or no data, in 1990 and so 1980 was used as the tidal analysis year for these stations. In practice the choice of the analysis year is not critical).

[39] The observed sea level for the 4 years not used for the tidal analysis can be written in the form

$$\eta = \eta_T + \eta_S + \eta_{R'} \tag{8}$$

where η_T is the predicted tide, η_S is the hindcast surge and $\eta_{R'}$ is the residual. Note the residual includes, as before, the effect of seiches and baroclinic effects not captured by the storm surge model. In addition, it also includes errors in predicting the tide based on data from another year. Thus $\eta_{R'}$ includes the differences in the low-frequency tides between the analyzed year and the predicted year.

[40] To reconstruct a total sea level record for the hindcast period we predict the tide using the tidal constants from the analysis year (e.g., 1990) and add it to the surge hindcast. To

include the effect of $\eta_{R'}$ we randomly sample with replacement from the 4 year $\eta_{R'}$ record in order to generate a realization of $\eta_{R'}$ for the complete hindcast period. It might be argued that such an approach does not allow for the serial dependence of $\eta_{R'}$. There are however theoretical results [e.g., *Leadbetter et al.*, 1983] that suggest limited-range dependence is not important for the distribution of extremes. (We confirmed this suggestion by decomposing some of the longest sea level records into tide and surge, randomly reordering the hourly surge values, and carrying out an extremal analysis on the sum of tides and reordered surges. We found that the return periods were effectively unchanged by the randomization step.)

[41] To allow for sampling variability of the reconstructed $\eta_{R'}$ we generated 10 such realizations for each station. This in turn gave 10 reconstructed total sea level records for the hindcast period. To estimate return periods we extracted, and ordered, the annual maxima for each realization. We then found a representative sequence of ordered annual maxima by taking the median across the 10 realizations. A Type I extremal analysis was then carried out on the medians to calculate the return periods at specified critical sea levels.

[42] Overall, the fit between the return periods calculated from the complete sea level records and the above approach, based on the surge hindcasts combined with information provided by 5 year sea level records, is good (compare Figures 5a and 5c). Most 40 year return levels from the short records are within about 10 cm of the observed return levels. Stations with large discrepancies are again those with short observation records.

4.2. Return Periods for Locations With No Sea Level Observations

[43] In principle, it is possible to use a limited area, dynamical model to calculate tides for any period if reasonable estimates of the open boundary conditions are available. This has been done for the shelf seas of Atlantic Canada by *Dupont et al.* [2002]. Excluding the Bay of Fundy, they estimate that the typical error in their tidal predictions is between 5 and 10 cm. Such tidal predictions for the hindcast period can then be combined with the surge hindcast to give a multidecadal reconstruction of total sea level which can then be subjected to standard extremal analysis.

[44] One problem is that it does not include the effect of $\eta_{R'}$. This can be overcome to some degree by using an $\eta_{R'}$ record from a nearby station in order to generate realizations for the hindcast period through random sampling as described in section 4.1. The success of this step is dependent on the representativeness of the nearby station with respect to $\eta_{R'}$. On an encouraging note we have fitted parametric forms of probability distributions (e.g., t-distributions) to the histograms of $\eta_{R'}$ and found that the parameters vary quite slowly within well-defined geographic regions like the southern Gulf of St. Lawrence or the Scotian Shelf. This suggests that within such regions, it may be possible to use representative $\eta_{R'}$ records to help calculate reasonable return periods for locations with no sea level data.

5. Conclusions

[45] In this study we used results from a 40 year hindcast of storm surges in the northwest Atlantic to calculate the return period of extreme sea levels. We were encouraged to find that the standard deviation of the hindcast error (the differences between the observed residuals and the surge hindcasts) is typically 8 cm and thus compares well with the operational forecast error for this region [*Bobanović et al.*, 2006]. The surge hindcasts also exhibited the same seasonal and interannual variations in standard deviation as the observed residuals. Having demonstrated the quality of the hindcast, we produced maps of the standard deviation of surges for the northwest Atlantic by season. As expected the surge variance was highest during the fall and winter [e.g., *Zhang et al.*, 2000]. We also showed that the regions with the highest surge variance were the southern Gulf of St Lawrence and the eastern shores of Newfoundland.

[46] Type I extremal analysis was performed on the annual maxima of the observed residuals and hindcast surges. Overall the agreement in the return periods of extreme levels is good although there was a tendency for the hindcast extreme surges to be too weak. (Similar hindcast projects, in Europe, have reported a similar underestimation of the largest storm events [e.g., *Kaas et al.*, 2001]). The agreement was nonetheless sufficiently good for us to produce, for the first time, maps of the 40 year return level of surges for the northwest Atlantic. The largest return levels were found in the southern Gulf of St. Lawrence and parts of the eastern shores of Newfoundland. This is of practical relevance because the southern Gulf of St. Lawrence is a region bounded by many low-lying areas known to be vulnerable to coastal flooding [e.g., *Thompson et al.*, 2002].

[47] To estimate the frequency of extreme total sea levels (in contrast to extreme surges) it is necessary to allow for the tide and ideally for other physical processes not resolved by the storm surge model. For locations with a few years of hourly sea level data this was achieved by predicting the tides for the hindcast period (based on the tidal analysis of one year of the hourly sea level observations) and adding them to the surge hindcast. We also allowed for the missing physics by randomly sampling from the differences between observed and predicted sea levels to generate realizations of prediction errors that were then added to the tide and surge hindcasts. Type I extremal analysis of the reconstructed total sea levels gave good estimates of the 40 year return level. An important point to note is that this approach requires only a few years of hourly sea level observations to estimate multidecadal return levels of total sea level. This method is an extension to that of *Pugh and Vassie* [1980] in which the observed sea level is first split into a tide and residual component. The histograms of each are then convolved to obtain a histogram of total sea levels under the assumption of no tide-surge interaction. In general the histogram from the convolution will be a more accurate representation of the histogram of a long sea level record than the histogram of a short observed sea level record. In our approach, adding the randomly sampled hindcast error, calculated from the short sea level record, is equivalent to the [*Pugh and Vassie*, 1980] convolution step. However, note that we are not adding back the observed residuals; we add the much smaller hindcast error. The extra information in our approach comes from using the surge hindcasts.

[48] When a dynamical tidal model is available it is possible to calculate tides anywhere in the domain and to combine them with the surge hindcasts. The return period of

extreme total sea levels at any location can then be estimated, including those with no sea level observations. This approach will generally underestimate slightly the return levels because of missing physics in the surge model. Preliminary results however suggest that the statistics of such errors are spatially uniform within well defined regions such as the Scotian Shelf. This means their contribution can be estimated from representative stations within the same region.

[49] It has been assumed throughout this study that tide-surge interaction is negligible in this region. This is consistent with the generally good estimates of the return levels of extreme residuals and total sea levels estimated for most of the tide gauge locations. It is nonetheless likely that allowing for tide-surge interaction, by including tidal forcing in the open boundary condition of the surge model, will improve the hindcasts of total sea level in some areas. Preliminary sensitivity studies suggest that tide-surge interaction may be significant in the southern Gulf of St. Lawrence. This study is continuing and will be the subject of a future publication.

[50] Secular trends in the observed annual maxima of total sea level were generally negative (see section 3.3). Although the majority of trends were not found to be significantly different from 0 at the 5% significance level, taken together they suggest that the region has undergone a slight decrease in extreme storm surges. Similar analysis performed on the annual pressure minima suggest that trends in annual pressure minima are a primary cause of the observed trend in sea level maxima (through the inverted barometer effect).

[51] The maps of surge standard deviation and 40 year return level for the northwest Atlantic differ significantly. More specifically, the return levels do not simply scale with the surge standard deviation. This means that there is no guarantee that a surge model that can accurately reproduce the surge standard deviation will be able to predict extreme surges. In general additional statistical properties of the surge histogram, such as skewness and kurtosis, can have an important effect on the return levels.

[52] The return levels presented here are based on a hindcast for a fixed observation period. It is possible however to extend the approach used here to allow for some elements of climate change. For example it is straightforward to approximate the effect of sea level rise by simply adding a constant amount to the return levels. Note however that in our study region it is not possible to add a spatially uniform rate of sea level rise; the effect of vertical crustal movements [*Peltier*, 2004] is spatially variable and of the same order as the generally accepted rate of global sea level rise of $1-2$ mm yr^{-1} [*Houghton et al.*, 2001].

[53] The most direct way of assessing how flooding risk might change over the next century is to run the surge model with high-resolution winds and air pressures fields from realistic climate change scenarios. Unfortunately the winds and air pressure fields available to us were too crude to accurately represent the intense storms that generate the large surges and therefore were not suitable for assessing the effect of climate change on flooding risk. We have however carried out some preliminary sensitivity studies of the impact of changes in surge distribution on flooding risk and compared the effect to that of sea level rise. On the basis of a plausible transformation of the surge histogram, reflecting plausible changes in storminess, we found that over the next century the largest contributor to increased flooding risk in the northwest Atlantic is sea level rise [*Bernier et al.*, 2006].

Appendix A: Dynamic Retrieval of the Pressure Fields

[54] The AES40 wind fields were produced with the ultimate goal of hindcasting North Atlantic waves and so no attention was paid to the calculation of the pressure fields. Pressure fields are however essential when modeling storm surges. Pressure fields from other reanalyses (e.g., NCEP/NCAR) were available but were too coarse for the study of extreme events. We therefore decided to infer the pressure fields from the AES40 wind fields.

[55] The theory for dynamic retrieval was first implemented by *Gal-Chen* [1978] and has since been used to generate pressure fields from Doppler radar observations [e.g., *Gal-Chen and Kropfli*, 1984; *Parsons et al.*, 1987; *Liou*, 2001]. In the present case, we assume that the horizontal pressure gradient above the planetary boundary layer is given by

$$-\frac{1}{\rho}\nabla p_a = \frac{\partial \mathbf{u}}{\partial t} + (\zeta + f)\mathbf{k}\times\mathbf{u} + \frac{1}{2}\nabla|\mathbf{u}|^2 \qquad \text{(A1)}$$

where p_a is the atmospheric pressure, $\mathbf{u}$ represents the gradient wind, f is the Coriolis parameter, ζ is the vorticity, and $\mathbf{k}$ is the upward pointing vector. The basic idea is to use the AES40 winds to calculate the right hand side of (A1) and thus to retrieve the pressure fields. This is done by first taking the divergence of (A1) to obtain an elliptic equation for pressure. All terms containing $\mathbf{u}$ are evaluated using AES40 surface winds. The elliptic equation is then solved up to an arbitrary constant of integration, using successive over-relaxation. Details of such numerical methods are readily available [e.g., *Press et al.*, 1986].

[56] A Dirichlet boundary condition was applied. It was imposed by evaluating the tangential form of (A1) at every point (along the boundary) for every time step. To uniquely specify the pressure along the open boundary, we had to specify the unknown constant of integration. We therefore assigned a pressure of 0 to one corner of our grid. Surface pressure observations from 5 land observing stations were then used to pin the pressure fields to the surface. The average pressure at the 5 grid points closest to the 5 observation stations were matched by a time-dependent offset. The offset was then applied to the integration constant thereby specifying the pressure fields.

[57] The difficulty in using AES40 winds to estimate the divergence of the right hand side of (A1) is that they do not represent gradient winds. The AES40 winds are 10 m winds. These surface winds must therefore be brought up through the planetary boundary layer before they can be used to solve the elliptic equation. To estimate a cross-isobar angle and a scaling, the following relationship between the gradient wind ($\mathbf{u}$) and the surface 10 m wind, $\mathbf{u_{10}}$ was assumed

$$\begin{bmatrix} u \\ v \end{bmatrix} = \alpha \begin{bmatrix} \cos\theta & \sin\theta \\ -\sin\theta & \cos\theta \end{bmatrix} \begin{bmatrix} u_{10} \\ v_{10} \end{bmatrix} + \begin{bmatrix} \epsilon_u \\ \epsilon_v \end{bmatrix} \qquad \text{(A2)}$$

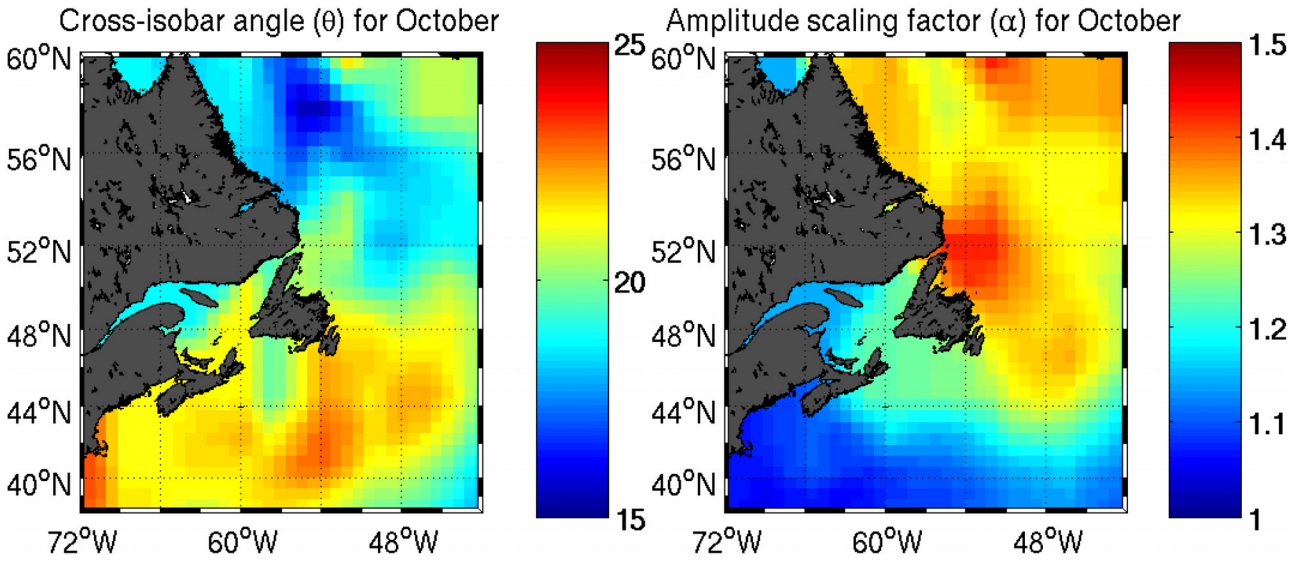

Figure A1. Relationship between the 10 m and gradient winds for October. (left) Cross-isobar angle in degrees. (right) Amplitude by which the rotated surface winds must be scaled to recover the gradient winds.

where α is a scaling factor and θ is a cross-isobar angle, estimated by minimizing the sum of the squared errors (ϵ_u and ϵ_v).

[58] In order to estimate the cross-isobar angles and amplitudes, the NCEP/NCAR 6-hourly reanalyzed surface wind and pressure fields were used [*Kalnay et al.*, 1996]. First, 6-hourly geostrophic winds were derived from the NCEP/NCAR pressure fields for the 1990–1999 period. The optimal cross-isobar angle (θ) and scaling factor (α) were then estimated by least squares for each month of the 10 year period. The parameters thus obtained vary smoothly from month to month and between years. The 10 values for each month of the year were therefore averaged to provide the cross-isobar angle and amplitude scaling factor for each month. Figure A1 shows the cross-isobar angle and the amplitude scaling factor for October.

[59] The α and θ were used to rotate the AES40 surface wind fields out of the planetary boundary layer thereby providing the winds necessary to solve for the pressure fields. 29 land stations and 23 CMAN and buoy records were used to validate the pressure fields. The RMS error of the predicted pressure field is 2.65 mb thereby validating the method presented here.

[60] **Acknowledgments.** We thank the Climate Change Action Fund and the Office of Critical Infrastructure Protection and Emergency Preparedness (OCIPEP) for financial support for the work reported on here. Part of this work was also funded by the Discovery Grant Program of the Natural Sciences and Engineering Research Council of Canada (NSERC). The authors acknowledge Val Swail for providing the high-resolution wind fields used in this study. The authors also thank R. Pawlowicz for his help using T_tide and Richard Peltier for sharing his ice-5G(VM2) model data. Finally, we would like to thank the reviewers for their constructive comments.

References

Bernier, N. B. (2005), Annual and seasonal extreme sea levels in the northwest Atlantic: Hindcasts over the last 40 years and projections for the next century, Ph.D. thesis, Dalhousie University, Halifax, N.S.

Bernier, N. B., K. R. Thompson, J. Ou, and C. H. Ritchie (2006), Mapping the return periods of extreme sea levels: Allowing for short sea level records, seasonality, and climate change, *Global Planet. Change*, in press.

Bobanović, J. (1997), Barotropic circulation variability on Canadian Atlantic shelves, Ph.D. thesis, Dalhousie University, Halifax, N.S.

Bobanović, J., K. R. Thompson, S. Desjardins, and H. Ritchie (2006), Forecasting storm surges along the east coast of Canada and the northeastern U.S.: The storm of 21 January 2000, *Atmos. Ocean*, *44*(2), 151–161.

Bowyer, P. J., and J. M. Gray (1995), *Where the Wind Blows: A Guide to Marine Weather in Atlantic Canada*, Breakwater, St. John's, Newfoundland.

Coles, S. (2001), *An Introduction to Statistical Modeling of Extreme Values*, *Springer Ser.*, *14*.

Davies, A. M., and R. A. Flather (1978), Application of numerical models of the north west European continental shelf and the North Sea to the computation of the storm surges of November to December 1973, *Dtsch. Hydrogr. Z.*, *A14*, 72 pp.

Dixon, M. J., and J. A. Tawn (1999), The effect of non-stationarity on extreme sea-level estimation, *J. R. Stat. Soc., Ser. C*, *48*, 135–151.

Dixon, M. J., J. A. Tawn, and J. M. Vassie (1998), Spatial modelling of extreme sea levels, *Environmetrics*, *9*, 283–301.

Dupont, F., C. G. Hannah, D. Greenberg, J. Cherniawsky, and C. E. Naimie (2002), Modelling system for tides for the northwest Atlantic coastal ocean, *Canadian Technical Report of Hydrography and Ocean Sciences 221*. (available online from the DFO library at http://www.dfo-mpo.gc.ca/Library/265855.pdf)

Flather, R. A., J. A. Smith, J. D. Richards, C. Bell, and D. L. Blackman (1998), Direct estimates of extreme storm surge elevations from a 40-year numerical model simulation and from observations, *Global Atmos. Ocean Syst.*, *6*, 165–176.

Gal-Chen, T. (1978), A method for the initialization of the anelastic equations: Implications for matching models with observations, *Mon. Weather Rev.*, *103*, 587–606.

Gal-Chen, T., and R. A. Kropfli (1984), Buoyancy and pressure perturbations derived from dual-Doppler radar observations of the planetary boundary layer: Applications for matching models with observations, *J. Atmos. Sci.*, *41*, 3007–3020.

Gill, A. E. (1982), *Atmosphere-Ocean Dynamics*, vol. 30, *Int. Geophys. Ser.*, Elsevier, New York.

Gumbel, E. (1958), *Statistics of Extremes*, Columbia Univ. Press, New York.

Houghton, J., Y. Ding, D. Griggs, M. Noguer, P. van der Linden, X. Dai, K. Maskell, and C. Johnson (Eds.) (2001), *Climate Change 2001: The Scientific Basis. Contribution of Working Group 1 to the Third Assessment Report of the Intergovernmental Panel on Climate Change*, Cambridge Univ. Press, New York.

Kaas, E., et al. (2001), *Regional storm, Wave and Surge Scenarios for the 2100 Century: Synthesis of the STOWASUS-2100 Project*, *Contract ENV4-CT97-0498*, Dan. Meteorol. Inst., Copenhagen.

Kalnay, E., et al. (1996), The NCEP/NCAR 40-year reanalysis project, *Bull. Am. Meteorol. Soc.*, *77*(3), 437–471.

Knippertz, P., U. Ulbrich, and P. Speth (2000), Changing cyclones and surface wind speeds over the north Atlantic and Europe in a transient GHG experiment, *Clim. Res.*, *15*(2), 109–122.

Lambert, S. (2004), Changes in winter cyclone frequencies and strengths in transient enhanced greenhouse warming simulations using two coupled climate models, *Atmos. Ocean*, *42*, 173–181.

Leadbetter, M., G. Lindgren, and H. Rootzen (1983), *Extremes and Related Properties of Random Sequences and Processes*, Springer, New York.

Liou, Y. C. (2001), The derivation of absolute potential temperature perturbations and pressure gradients from wind measurements in three-dimensional space, *J. Atmos. Oceanic Technol.*, *18*(4), 577–590.

Lowe, J. A., J. M. Gregory, and R. A. Flather (2001), Changes in the occurrence of storm surges around the United Kingdom under a future climate scenario using a dynamic storm surge model driven by the Hadley Centre climate models, *Clim. Dyn.*, *18*(3–4), 179–188.

Mellor, G. L. (1998), Users guide for a three-dimensional, primitive equation, numerical ocean model, technical report, Princeton University, Princeton, N.J.

Milne, G. A., J. L. Davis, J. X. Mitrovica, H.-G. Scherneck, J. M. Johansson, M. Vermeer, and J. Koivula (2001), Space-geodetic constraints on glacial isostatic adjustment in Fennoscandia, *Science*, *291*, 2381–2385.

Parsons, D. B., C. G. Mohr, and T. Gal-Chen (1987), A severe frontal rain band. part III: Derived thermodynamic structure, *J. Atmos. Sci.*, *44*(12), 1615–1631.

Pawlowicz, R., B. Beardsley, and S. Lentz (2002), Classical tidal harmonic analysis including error estimates in MATLAB using T-Tide, *Comput. Geosci.*, *28*(8), 929–937.

Peltier, W. R. (2004), Global glacial isostasy and the surface of the ice-age Earth: The ice-5G (VM2) model and Grace, *Ann. Rev. Earth Planet. Sci.*, *32*, 111–149.

Press, W., B. Flannery, S. Teukolsky, and W. Vetterling (1986), *Numerical Recipes: The Art of Scientific Computing*, Cambridge Univ. Press, New York.

Pugh, D. T., and J. M. Vassie (1980), Application of the joint probability method for extreme sea level computations, *Proc. Inst. Civ. Eng., Part 2*, *69*, 959–975.

Pugh, D. T. (1987), *Tides, Surges and Mean Sea Level*, John Wiley, Hoboken, N. J.

Soares, C. G., R. Weisse, J. C. Carretero, and E. Alvarez (2002), A 40 years hindcast of wind, sea level and waves in European waters, paper OMAE2002-SR28604 presented at the 21st International Conference on Offshore Mechanics and Arctic Engineering, Am. Soc. of Mech. Eng., Oslo, June 23–28.

Stollhofen, H., I. G. Stanistreet, B. Bangert, and H. Grill (2000), Tuffs, tectonism and glacially related sea level changes, Carboniferous-Permian, southern Namibia, *Paleogeogr. Palaeoclimatol. Palaeoecol.*, *161*, 127–150.

Swail, V. R., and A. T. Cox (2000), On the use of NCEP-NCAR reanalysis surface marine wind fields for a long-term North Atlantic wave hindcast, *J. Atmos. Ocean Tech.*, *17*, 532–545.

Swail, V. R., E. A. Ceccafi, and A. T. Cox (2000), The AES40 North Atlantic wave reanalysis: Validation and climate assessment, paper presented at 6th International Workshop on Wave Hindcasting and Forecasting, Monterey, Calif. (Available online at http://www.oceanweather.net/about/papers/index.html)

Tawn, J. A., and J. M. Vassie (1989), Extreme sea levels: The joint probability method revisited and revised, *Proc. Inst. Civ. Eng., Part 2*, *87*, 429–442.

Thompson, K., H. Ritchie, N. Bernier, J. Bobanović, S. Desjardins, P. Pellerin, W. Blanchard, B. Smith, and G. Parkes (2002), *Coastal Impacts of Climate Change and Sea Level Rise on Prince Edward Island. Appendix2: Modelling Storm Surges and Flooding Risk at Charlottetown*, *Tech. Rep. GB 459.6 6.M42 (CD-ROM) Open File 4261*, Geol. Surv. of Canada, Ottawa, Ont.

Thompson, K. R., J. Y. Sheng, P. C. Smith, and L. Z. Cong (2003), Prediction of surface currents and drifter trajectories on the inner Scotian shelf, *J. Geophys. Res.*, *108*(C9), 3287, doi:10.1029/2001JC001119.

Unnikrishnan, A. S., D. Sundar, and D. L. Blackman (2004), Analysis of extreme sea level along the east coast of India, *J. Geophys. Res.*, *109*, C06023, doi:10.1029/2003JC002217.

Woodworth, P. L., and D. L. Blackman (2002), Changes in extreme high waters at Liverpool since 1768, *Int. J. Clim.*, *22*(6), 697–714.

Zhang, K. Q., B. C. Douglas, and S. P. Leatherman (2000), Twentieth-century storm activity along the U.S. east coast, *J. Clim.*, *13*, 1748–1761.

N. B. Bernier and K. R. Thompson, Department of Oceanography, Dalhousie University, 1355 Oxford Street, Halifax, Nova Scotia, B3H 4J1, Canada. (natacha.bernier@phys.ocean.dal.ca; keith.thompson@dal.ca)